GEOPHYSICS, VOL. 84, NO. 1 (JANUARY-FEBRUARY 2019); P. S29–S40, 14 FIGS., 1 TABLE.
10.1190/GEO2017-0850.1

Joint least-squares reverse time migration of primary and prismatic waves

Jizhong Yang[1], Yuzhu Liu[2], Yunyue Elita Li[3], Arthur Cheng[3], Liangguo Dong[2], and Yue Du[3]

ABSTRACT

Direct imaging of the steeply dipping structures is challenging for conventional reverse time migration (RTM), especially when there are no strong reflectors in the migration velocity model. To address this issue, we have enhanced the imaging of the steeply dipping structures by incorporating the prismatic waves. We formulate the imaging problem in a nonlinear least-squares optimization framework because the prismatic waves cannot be linearly mapped from the model perturbation. Primary and prismatic waves are jointly imaged to provide a single consistent image that includes structures illuminated by both types of waves, avoiding the complexities in scaling and/or interpreting primary and prismatic images separately. A conjugate gradient algorithm is used to iteratively solve the least-squares normal equation. This inversion procedure can become unstable if directly using the recorded data for migration because it is hindered by the crosstalk caused by imaging primary waves with the prismatic imaging operator. Therefore, we isolate the prismatic waves from the recorded data and image them with the prismatic imaging operator. Our scheme only requires a kinematically accurate and smooth migration velocity model, without the need to explicitly embed the strong reflectors in the migration velocity model. Realistic 2D numerical examples demonstrate that our method can resolve the steeply dipping structures much better than conventional least-squares RTM of primary waves.

INTRODUCTION

Detection of steeply dipping structures, such as vertical or nearly vertical faults and salt flanks, plays an important role in well planning, drilling, and risk assessment for oil and gas exploration. However, high-resolution imaging of these structures is challenging. Conventional methods rely on singly scattered events, but such events that illuminate steeply dipping reflectors are seldom recorded at the surface (Figure 1a). Turning waves, for example, can make a significant contribution for imaging these targets (Hale et al., 1992; Xu and Jin, 2006), but they may not be present in the data when strong velocity gradient is lacking, or the acquisition aperture is limited.

Prismatic waves, known as duplex waves, also illuminate the steeply dipping structures and are often recorded even when acquisition aperture is limited. For the purpose of this study, we define the prismatic waves as doubly scattered waves, which reflect from two near-orthogonal interfaces before reaching the receiver on the surface, as illustrated in Figure 1b. Compared with primary waves, prismatic waves carry reflection information from steeply dipping interfaces. We assume that all arrivals that are not singly scattered or prismatic waves, including refracted waves and other types of multiply reflected waves, are removed from the recorded data.

Migration of prismatic waves for delineation of the steeply dipping structures has been studied by many researchers and can be summarized into two categories. The first category is to explicitly embed the sharp reflectors into the migration velocity model (Marmalyevskyy et al., 2005; Farmer et al., 2006; Jin et al., 2006; Jones et al., 2007; Li et al., 2011). However, accurate positioning of the sharp reflectors adds complexity to the already difficult migration velocity model building process. The other category is to use the migration image of primary waves to generate back-scattered wavefield, avoiding the modification of the migration velocity model

---

Manuscript received by the Editor 27 December 2017; revised manuscript received 14 September 2018; published ahead of production 31 October 2018; published online 21 December 2018.

[1] Formerly Tongji University, State Key Laboratory of Marine Geology, Shanghai 200092, China; presently National University of Singapore, Department of Civil and Environmental Engineering, Singapore 119077, Singapore. E-mail: ceeyaj@nus.edu.sg.

[2] Tongji University, State Key Laboratory of Marine Geology, Shanghai 200092, China. E-mail: liuyuzhu@tongji.edu.cn (corresponding author); dlg@tongji.edu.cn.

[3] National University of Singapore, Department of Civil and Environmental Engineering, Singapore 119077, Singapore. E-mail: ceeliyy@nus.edu.sg; ceeccha@nus.edu.sg; ceeydu@nus.edu.sg.

(Malcolm et al., 2009, 2011; Dai and Schuster, 2013; Zuberi and Alkhalifah, 2013, 2014). The images from primary waves and prismatic waves are then summed together with empirically chosen weighting coefficients for subsequent geologic interpretation.

The migration methods mentioned above are performed by applying the adjoint of the forward-modeling operator to the recorded seismic data. This is not always a good approximation for the inverse of the forward-modeling operator required to retrieve the true reflection coefficients (Claerbout, 1992). As a consequence, the final image may suffer from migration artifacts, providing a blurred description of the subsurface reflectivity distribution with distorted amplitudes. This result is mainly caused by limited recording apertures, under-sampled acquisition geometry, band-limited source wavelet, and uneven subsurface illumination.

To improve the quality of the migrated images and to mitigate the artifacts, Aldawood et al. (2014, 2015) propose a Kirchhoff-based least-squares migration (LSM) method for imaging prismatic waves. They use the image from LSM of primary waves as a constraint to linearize the forward modeling and adjoint operators for LSM of prismatic waves. The images from these two steps are then stacked for subsequent geologic interpretation. This method eliminates the need for estimating an empirical weight for summation because the relatively accurate reflection coefficients are obtained through LSM. Nevertheless, owing to the high-frequency approximation for the ray-based Kirchhoff migration method, it cannot handle complicated subsurface structures, such as salt flanks, which are important geologic features for oil and gas exploration and production.

Tan and Huang (2014) propose a least-squares reverse time migration (LSRTM) method that directly images steeply dipping fault zones with a wavefield-separation imaging condition. It also updates the migration velocity model, and hence the source wavefields, at each iteration. The recalculation of the source wavefields accounts for the multiple reflections from faults that are weaker than primary reflections. However, the velocity model is updated based on the migration image, which is contaminated by artifacts, and thus it slows the convergence. They also propose to switch the imaging condition from the total migration image to the horizontal-looking image, but this can only be achieved empirically.

In this study, we propose an LSRTM scheme that jointly images primary and prismatic waves, abbreviated as JLSRTM hereafter. The distinction between our JLSRTM and conventional LSRTM of primary waves is that the relationship between the modeled data and the subsurface model perturbation is no longer linear. The output of JLSRTM is a single consistent image that includes structures illuminated by primary and prismatic waves, avoiding the complexities in scaling and/or interpreting primary and prismatic images separately. A conjugate gradient algorithm is used to iteratively solve the least-squares normal equation. Theoretical analysis and numerical observations indicate that the crosstalk artifacts resulting from the imaging of primary waves as prismatic waves occur if the recorded data are directly used for migration, making the inverse procedure unstable. A potential solution to this instability is to separate the prismatic waves from the recorded data and to image them properly with the prismatic imaging operator. A kinematically accurate and smooth migration velocity model is needed to obtain focused images, but it is unnecessary to modify the smooth migration velocity model to include the sharp subhorizontal reflectors or to update the migration velocity model throughout the iterative inverse procedure.

The rest of this paper is organized as follows. In the "Methodology" section, we describe the formulation of JLSRTM. In the "Numerical example" section, we first use a simple "L" model to show the capability of our JLSRTM to image vertical structures. Then, we further demonstrate the effectiveness of our method on a salt-like model and the SEG Advanced Modeling (SEAM) model. Finally, we discuss the implications of our method to the field data application.

METHODOLOGY

In the frequency domain, the acoustic-wave equation with constant density is expressed as

$$-\omega^2 m(x)u(x,\omega;x_s) - \nabla^2 u(x,\omega;x_s) = \delta(x-x_s)f(\omega), \tag{1}$$

where ω is the angular frequency, $f(\omega)$ is the source signature at the source location x_s, $m(x) = 1/v^2(x)$ is the squared slowness, and $u(x,\omega;x_s)$ is the frequency-domain pressure wavefield. A perturbation in the model $m(x) = m_0(x) + \delta m(x)$ leads to a perturbation in the wavefield $u(x,\omega;x_s) = u_0(x,\omega;x_s) + \delta u(x,\omega;x_s)$.

The background squared slowness $m_0(x)$ and the corresponding background wavefield $u_0(x,\omega;x_s)$ satisfy the following wave equation:

$$-\omega^2 m_0(x)u_0(x,\omega;x_s) - \nabla^2 u_0(x,\omega;x_s) = \delta(x-x_s)f(\omega). \tag{2}$$

Substituting the model perturbation and wavefield perturbation into equation 1 and combining with equation 2, we obtain

$$\begin{aligned}&-\omega^2 m_0(x)\delta u(x,\omega;x_s) - \nabla^2 \delta u(x,\omega;x_s)\\ &\quad = \omega^2 \delta m(x)u_0(x,\omega;x_s) + \omega^2 \delta m(x)\delta u(x,\omega;x_s).\end{aligned} \tag{3}$$

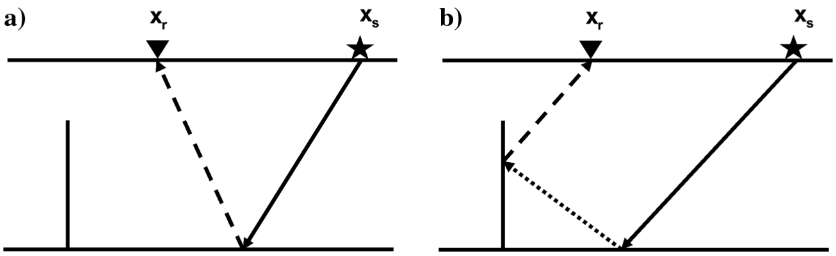

Figure 1. Schematic illustration of (a) a primary raypath that reflects from a single interface and (b) a prismatic raypath that reflects from two interfaces with different dips.

For the purpose of this study, we argue that when there exists steeply dipping structures, such as the vertical or nearly vertical faults and salt flanks in the subsurface, the model perturbation will lead to the wavefield perturbation including singly and doubly scattered waves $\delta u(x,\omega;x_s) = \delta u_1(x,\omega;x_s) + \delta u_2(x,\omega;x_s)$, with $\delta u_1(x,\omega;x_s)$ denoting the singly scattered waves, and $\delta u_2(x,\omega;x_s)$ indicating the doubly scattered waves. All the higher order terms, such as the triply scattered waves, are neglected. Substituting the wavefield perturbation into equation 3, we obtain

$$
\begin{aligned}
&-\omega^2 m_0(x)\delta u_1(x,\omega;x_s) - \nabla^2 \delta u_1(x,\omega;x_s) \\
&\quad - \omega^2 m_0(x)\delta u_2(x,\omega;x_s) - \nabla^2 \delta u_2(x,\omega;x_s) \\
&\quad = \omega^2 \delta m(x) u_0(x,\omega;x_s) + \omega^2 \delta m(x)\delta u_1(x,\omega;x_s) \\
&\quad\quad + \omega^2 \delta m(x)\delta u_2(x,\omega;x_s).
\end{aligned} \tag{4}
$$

We separate equation 4 into two parts:

$$
\begin{aligned}
&-\omega^2 m_0(x)\delta u_1(x,\omega;x_s) - \nabla^2 \delta u_1(x,\omega;x_s) \\
&\quad = \omega^2 \delta m(x) u_0(x,\omega;x_s),
\end{aligned} \tag{5}
$$

$$
\begin{aligned}
&-\omega^2 m_0(x)\delta u_2(x,\omega;x_s) - \nabla^2 \delta u_2(x,\omega;x_s) \\
&\quad = \omega^2 \delta m(x) \delta u_1(x,\omega;x_s),
\end{aligned} \tag{6}
$$

in which the term $\omega^2\delta m(x)\delta u_2(x,\omega;x_s)$ is dropped because it is of a higher order when compared with $\omega^2\delta m(x)u_0(x,\omega;x_s)$ and $\omega^2\delta m(x)\delta u_1(x,\omega;x_s)$. The relation between the singly scattered wave $\delta u_1(x,\omega;x_s)$ and the model perturbation $\delta m(x)$ is linear, whereas the relation between the doubly scattered wave $\delta u_2(x,\omega;x_s)$ and the model perturbation $\delta m(x)$ is nonlinear, as $\delta u_1(x,\omega;x_s)$ is also a function of $\delta m(x)$.

We assume that the recorded scattering data δd contain primary reflection waves δd_1 and doubly scattered prismatic waves δd_2, that is,

$$\delta d = \delta d_1 + \delta d_2. \tag{7}$$

The transmitted waves, such as the direct arrival, refractive waves, and diving waves are muted. We neglect all the surface-related and internal multiples, and we assume that they are sufficiently attenuated by preprocessing (Verschuur et al., 1992; Berkhout and Verschuur, 1997; Weglein et al., 1997; Jakubowicz, 1998).

Conventional LSRTM aims to solve model perturbation δm by minimizing the difference between the forward modeled data $R\delta u_1$ and the recorded data δd in a least-squares sense:

$$J(\delta m) = \frac{1}{2}\|R\delta u_1 - \delta d\|_2^2, \tag{8}$$

where R is the sampling operator at the receiver location.

Under the single-scattering assumption, LSRTM can suppress the migration artifacts and enhance the seismic reflectors that are mainly illuminated by primaries. The prismatic waves and other multiples, such as surface-related or internal multiples, are treated as noise and cannot be properly imaged.

To take into account the prismatic wave for subsurface imaging, we formulate a joint LSRTM as a nonlinear optimization problem:

$$J(\delta m) = \frac{1}{2}\|R\delta u_1 + R\delta u_2 - \delta d\|_2^2. \tag{9}$$

We choose this nonlinear formulation to obtain a single consistent image that includes structures illuminated by primary and prismatic waves, avoiding the complexities in scaling and/or interpreting the primary and the prismatic images separately.

The minimizer of equation 9 can be found when $\partial J(\delta m)/\partial \delta m = 0$, resulting in the following normal equation:

$$H\delta m = m_{\mathrm{mig}}, \tag{10}$$

where H is the Hessian operator and m_{mig} is the standard reverse time migration (RTM) image. We give detailed derivations of equation 10 in Appendix A. Imaging conditions for migration of primary and prismatic waves are clearly defined in Appendix B.

In Appendix C, we reformulate the least-squares normal equation in equation 10 with the assumption that isolation of prismatic waves from the recorded data is readily available, through which the crosstalk artifacts resulting from the mistaken crosscorrelation between the singly and doubly scattered energies are clearly identified and explicitly dropped off. A conjugate gradient method (Hestenes and Stiefel, 1952) is then used to iteratively solve the reformulated normal equation in Appendix C.

The isolation of prismatic waves from the recorded data is not straightforward. In the numerical examples, we separate the prismatic waves from the recorded data by subtracting the Born modeled data (approximated primary data) based on the conventional LSRTM image. We also show comparisons when the prismatic imaging operator is applied on all recorded data and on the predicted prismatic data.

The workflow of our JLSRTM is as follows:

1) Generate a conventional LSRTM migrated model.
2) Calculate the primary reflection data predicted from the migrated model in step 1.
3) Subtract the primary reflection data in step 2 from the full recorded scattering data to obtain an estimate of the prismatic waves.
4) Update the model perturbation by solving the normal equation 10 using a conjugate gradient algorithm (Hestenes and Stiefel, 1952), in which the Hessian-vector product is calculated using Algorithm C-1.

NUMERICAL EXAMPLES

To validate our JLSRTM algorithm in delineating the vertical structures, we perform tests on a simple L model, a "cartoon" salt-like model, and the SEAM Phase I Subsalt Earth Model. Although we present the derivations in the frequency domain for simplicity, the actual implementations are in the time domain. Synthetic seismic data are generated by solving the acoustic-wave equation using the temporal second-order and spatial fourth-order finite-difference method, with perfectly matched layer absorbing boundary condition implemented on four sides of the model (Hu et al., 2007). The synthetic data contain not only primary and prismatic reflections but also refracted waves, diving waves, and internal multiples if they are permitted by the model. No surface-related multiples or ghosts are included in the data.

The L model

We first apply our method to a simple L model (Dai and Schuster, 2013) (Figure 2a) that contains a horizontal reflector and a vertical reflector. The model grid is 201 × 151 in size, with a grid interval of 10 m. The acquisition system consists of 49 sources and 201 receivers on the surface, spaced at 40 and 10 m intervals, respectively. The source function is a Ricker wavelet with a peak frequency of 30 Hz. The recording time is 3.0 s with a time interval of 1 ms. Figure 2b shows the observed data for the 24th shot located at (1000 m, 0 m), with the direct arrival muted. There are three main events: the diffraction from the top of the vertical structure, the primary reflection from the horizontal reflector, and the prismatic wave reflected twice from the horizontal and vertical reflectors. The migration velocity model is a constant background velocity model. Figure 3a shows the RTM image, and Figure 3b shows the conventional LSRTM image. The conventional LSRTM provides better images than the RTM in terms of better amplitude balancing and resolution enhancement. However, the vertical structures are invisible in the conventional LSRTM and RTM images. The Born modeled data from the conventional LSRTM image and the data residual, together with the observed data, are shown in Figure 4. It is evident that only the diffraction and primary reflection are well-predicted by conventional LSRTM, whereas the prismatic waves remain in the data residual.

Before showing the JLSRTM results, we first analyze the influence of the primary waves on the imaging of prismatic waves as discussed in Appendix B. Figure 5a shows the migration image of prismatic waves, in which all the recorded data are injected for the receiver-side backpropagation. To generate this image, the conventional RTM image shown in Figure 3a is used to calculate the source- and receiver-side scattered wavefields. Compared with Figure 3a, the vertical structure is now visible. This indicates that the prismatic wave components in the recorded data can be used to image the vertical structures if proper imaging condition is used. However, strong artifacts occur: The horizontal reflector and the diffraction point at the top of the vertical structure are actually calculated from the term in equations B-3 and B-5. They have incorrect polarity and higher frequency content compared with the conventional RTM image in Figure 3a, which is calculated using the term on the right side of equation B-1. These artifacts will affect the subsequent data fitting in the inversion procedure.

For comparison, the migration image using the predicted prismatic waves (Figure 4c) is displayed in Figure 5b. This image is calculated using the term in equations B-4 and B-6. Only the vertical structure is retrieved. In other words, if we want to locate the steeply dipping structures with the prismatic waves free of artifacts caused by primary waves, the prismatic waves should be isolated from the recorded data, or at least the primary waves should be attenuated.

Figure 5c shows the image of JLSRTM, in which all the recorded seismic data are used as prismatic waves for receiver-side backpropagation. The vertical and horizontal reflectors are simultaneously resolved in the image, with weaker amplitude for the vertical reflector. This result cannot be further improved because the inversion becomes unstable after 15 iterations. The corresponding data residual (Figure 6c) shows that not only the prismatic reflection is barely predicted, but the high-wavenumber crosstalk artifacts on the horizontal reflector also introduce more error for the primary reflection. Both effects hamper the iterative inverse process.

To mitigate the crosstalk artifacts and stabilize the inversion, we first predict the prismatic reflections (Figure 4c) by subtracting the Born modeled data (Figure 4b) based on the conventional LSRTM image (Figure 3b) from the recorded data (Figure 4a). The corresponding JLSRTM result is displayed in Figure 5d. It is obvious that the image of the vertical structure is enhanced with stronger amplitude and better continuity. Figure 6d shows the data residual of JLSRTM with separated prismatic reflections. Compared with conventional LSRTM (Figure 6b) and JLSRTM with all recorded data as prismatic waves (Figure 6c), JLSRTM with separated prismatic reflections can better predict all the seismic events and achieve better convergence. Therefore, only the JLSRTM images with separated prismatic waves are illustrated in the following numerical examples.

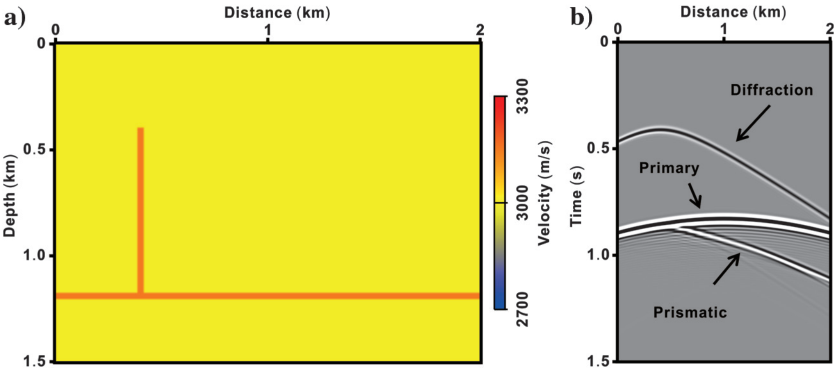

Figure 2. (a) The true velocity for L model and (b) the corresponding shot gather generated using the finite-difference method for the 24th shot located at (1000 m, 0 m).

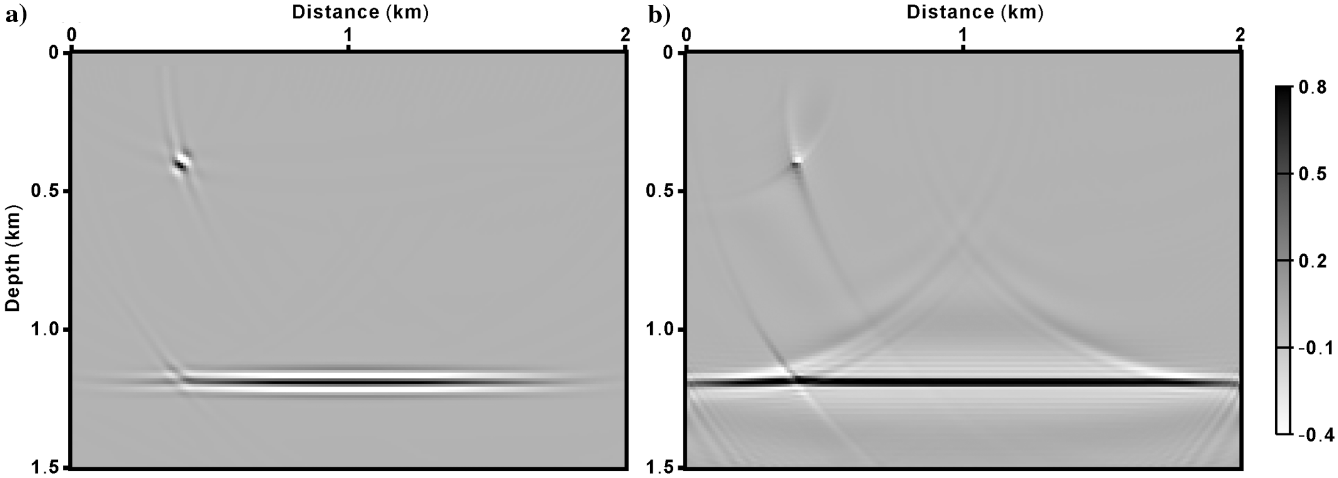

Figure 3. Images from (a) the RTM and (b) the conventional LSRTM.

The salt-like model

We then test the proposed method on a cartoon salt-like model shown in Figure 7a. It has four horizontal layers and a salt body in the middle. The model dimensions are of 401 × 151, with 10 m grid intervals. There are 79 shots evenly spaced at 50 m shot intervals, and each shot is recorded with 401 receivers evenly distributed at 10 m receiver spacing. The sources and receivers are on the surface, with the first source and receiver located at distances of 50 and 0 m, respectively. The source function is a Ricker wavelet with a peak frequency of 30 Hz. The recording time is 2.5 s, with a time interval of 0.5 ms. The migration velocity model only contains the smoothed salt body in the homogeneous background velocity as shown in Figure 7b. Figure 8a and 8b shows the conventional RTM and LSRTM images, in which the salt flanks are not well-delineated, although the LSRTM provides better result than the RTM with balanced amplitudes and enhanced spatial resolution for the horizontal reflectors. The JLSRTM image is shown in Figure 8c. The salt flanks are better revealed with coherent structure and amplitudes. The magnified views of the gray boxes in Figure 8 are shown in Figure 9. It is evident that the salt flanks are more continuously imaged and the polarities are more accurate in the JLSRTM image.

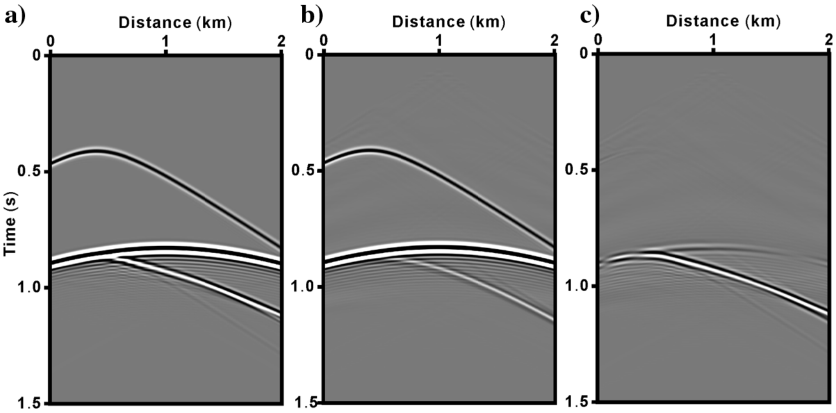

Figure 4. Seismogram of (a) the recorded data, (b) the forward Born modeled data based on the conventional LSRTM image shown in Figure 3b, and (c) the data residual for the 24th shot located at (1000 m, 0 m).

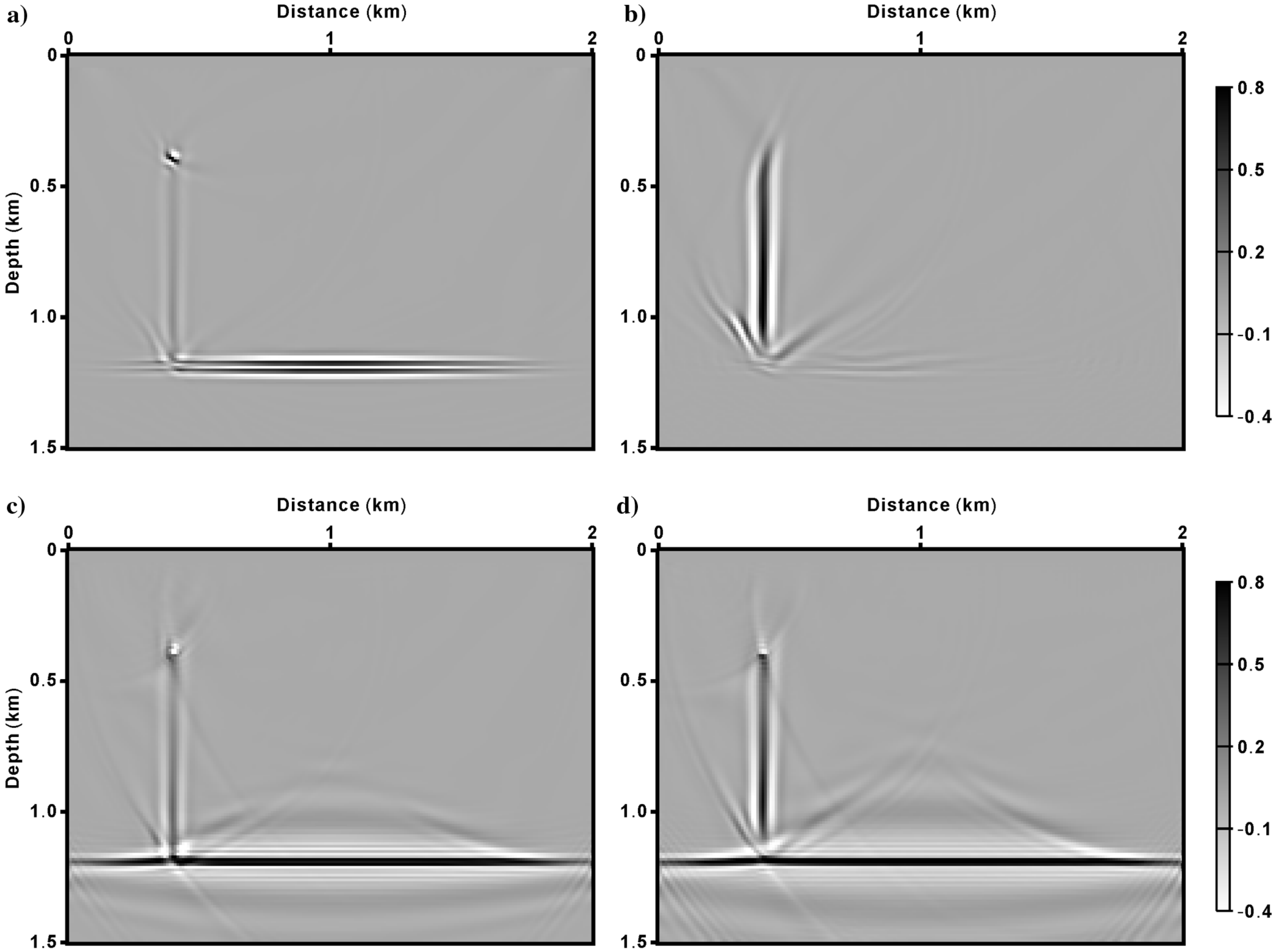

Figure 5. Images from (a) the migration of the prismatic wave, in which the recorded data are regarded as the prismatic wave, (b) the migration of the prismatic wave, in which the primary wave is eliminated from the recorded data, (c) the JLSRTM with the recorded data injected for the receiver-side backpropagation, and (d) the JLSRTM with the separated prismatic waves injected for the receiver-side backpropagation.

SEAM model

We further demonstrate our method with the SEAM model. The SEAM model is a 3D representation of a deepwater Gulf of Mexico salt domain, completed with fine-scale stratigraphy and fluid-filled reservoirs (Fehler and Keliher, 2011). We use a 2D east–west cross section at north = 23,900 m in the 3D SEAM model. To decimate the original model, we take one parameter value for each of four grid points and set the discretization grid as 20 m. This results in a coarse model of 438 × 376 in size. The resulting velocity model is presented in Figure 10a. It has a complex rugose salt body, with overhangs and steep flanks on its east and west sides. There are 86 shots evenly spaced at 100 m shot intervals, and each shot is recorded with 438 receivers evenly distributed at 20 m receiver spacing. The sources and receivers are on the surface, with the first source and receiver located at distances of 100 and 0 m, respectively. The source function is a Ricker wavelet with a peak frequency of 10 Hz. The recording time is 6.0 s, with a time interval of 2 ms. The migration velocity model (Figure 10b) is built by smoothing the true velocity model (Figure 10a) with a 2D Gaussian function whose vertical and horizontal correlation lengths are 200 m. We keep the velocity models greater than 1.4 km (denoted by the white line) fixed as in the true velocity model. This is consistent with industry practice wherein the top of salt is "picked" and "frozen" before migrating deeper structures.

For this particular case, the observed seismic data are generated by solving the acoustic-wave equation with variable density using staggered-grid finite-difference method:

$$-\frac{\omega^2}{\rho(x)v^2(x)}u(x,\omega;x_s)-\nabla\cdot\left[\frac{1}{\rho(x)}\nabla u(x,\omega;x_s)\right]=\delta(x-x_s)f(\omega), \tag{11}$$

where ρ is the density. In this study, the density model (Figure 10c) is decimated from the original SEAM density model using the same parameters for decimation of velocity model stated previously. In addition, we add random Gaussian noise to the recorded data using the Seismic Unix software *suaddnoise* with sn = 5. The resulting signal-to-noise ratio is 0.3, defined as

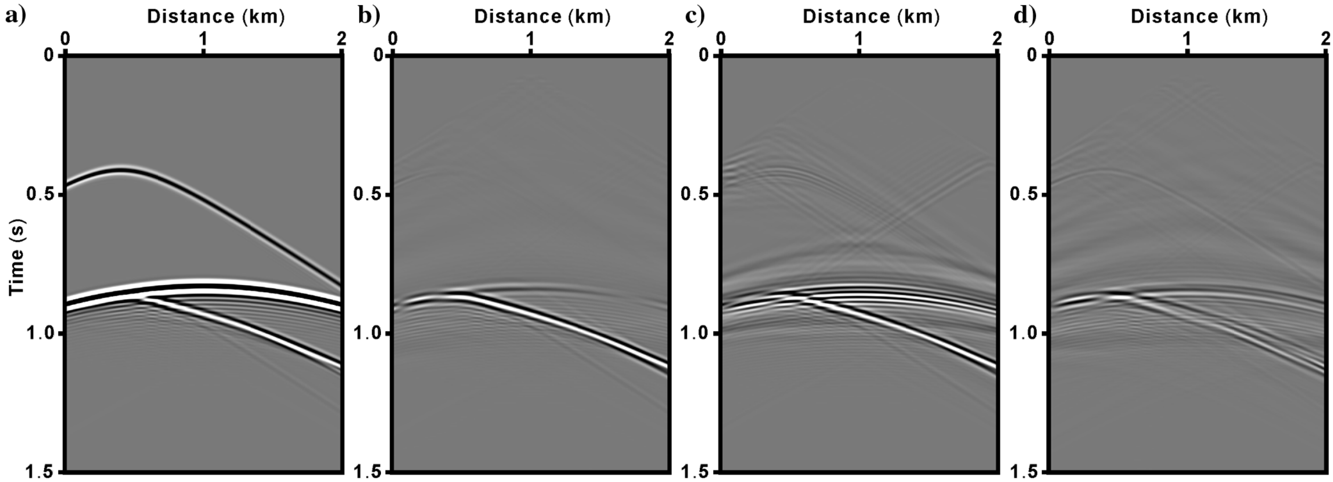

Figure 6. The seismogram of (a) the recorded data, (b) the data residual after conventional LSRTM, (c) the data residual after joint LSRTM without separation, and (d) the data residual after joint LSRTM using the approximately separated prismatic waves for the 24th shot located at (1000 m, 0 m).

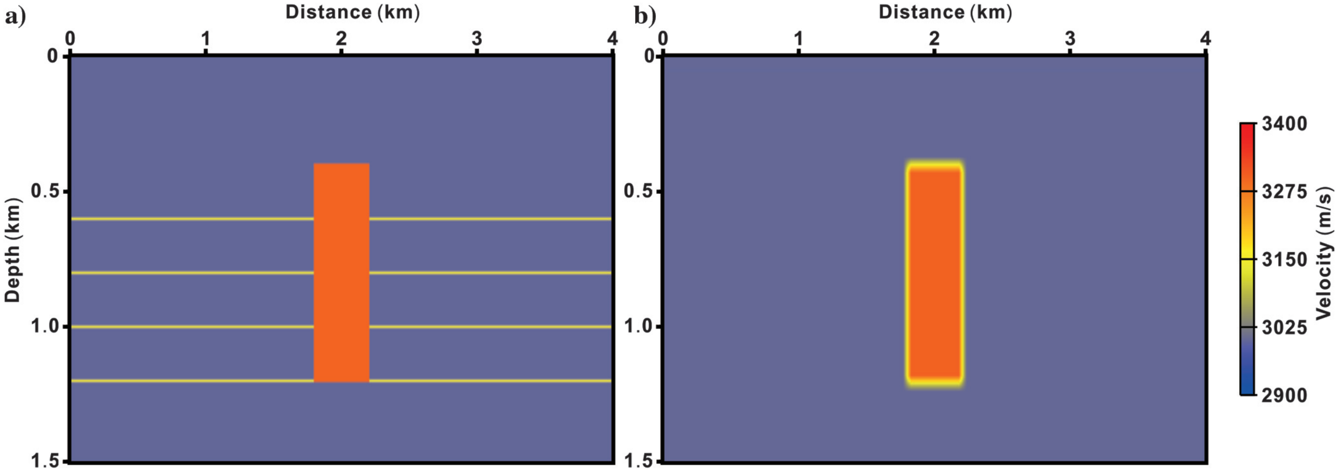

Figure 7. The salt-like model: (a) the true velocity model for data simulation and (b) the accurate migration velocity model.

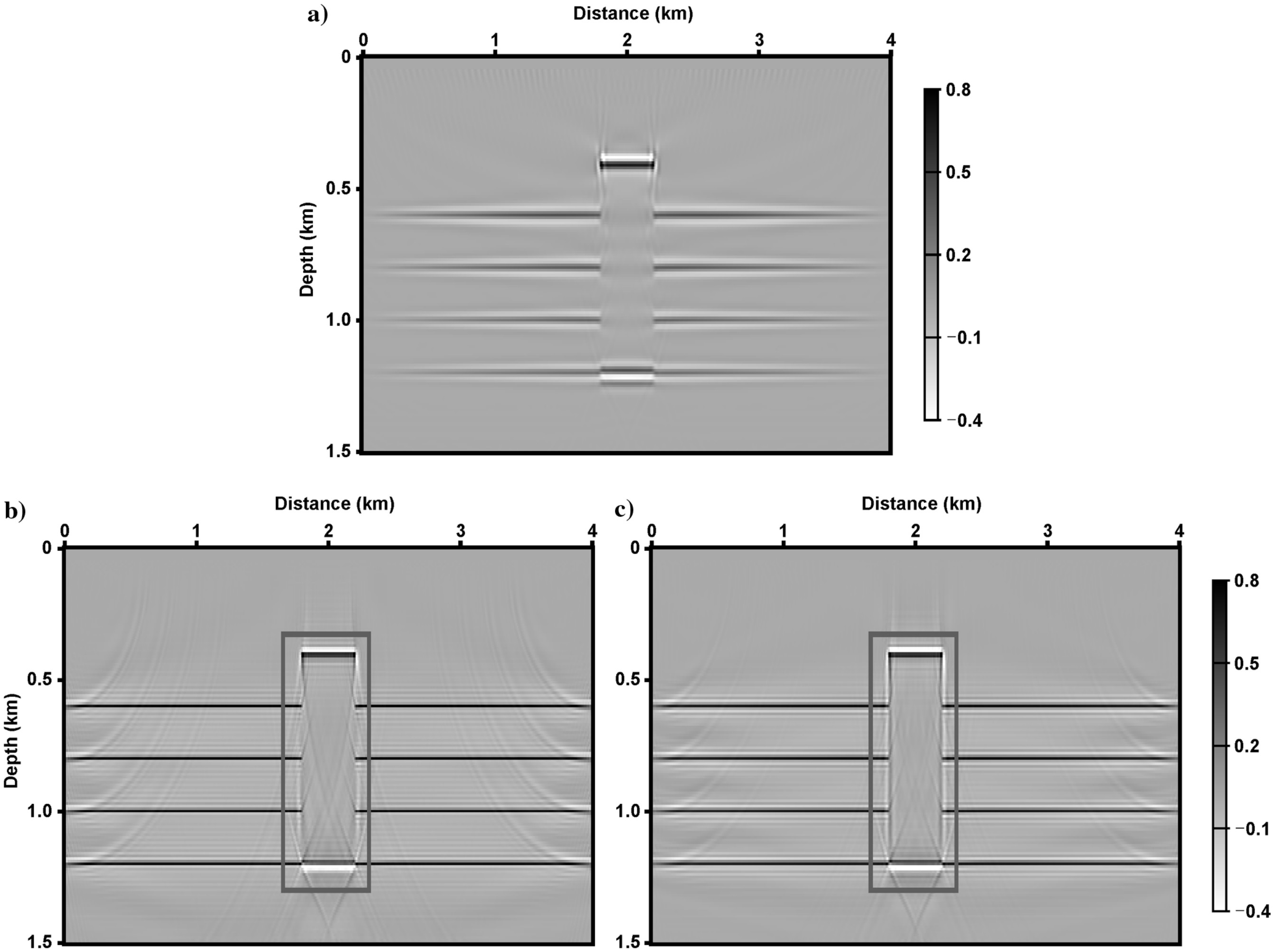

Figure 8. Images from (a) RTM, (b) conventional LSRTM, and (c) JLSRTM for the salt-like model. The gray boxes point to the areas for the magnified views.

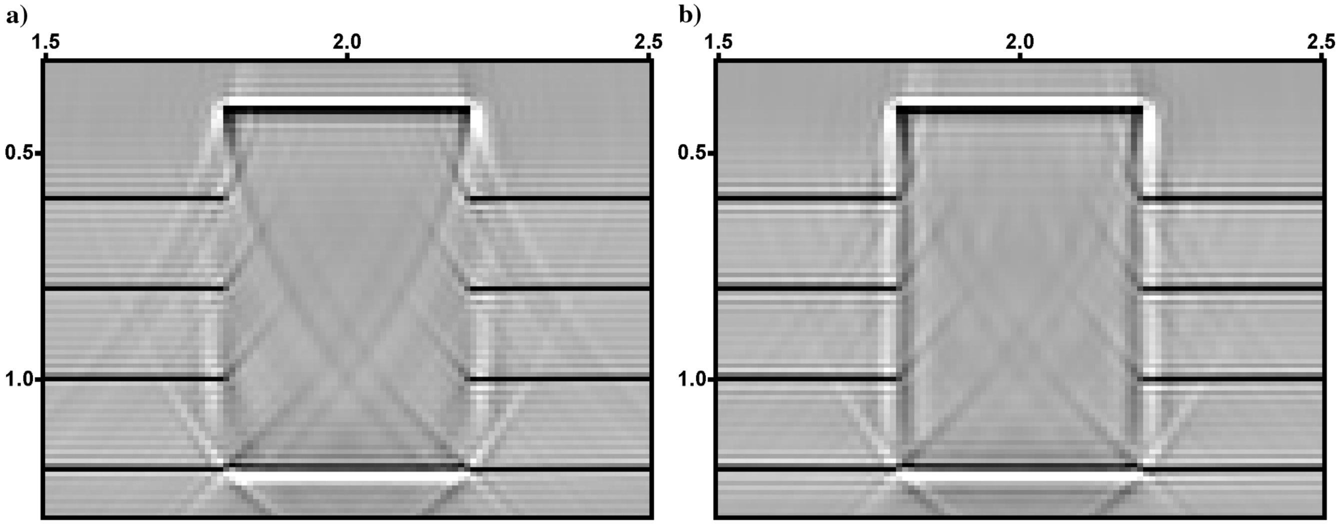

Figure 9. Magnified views of the gray boxes in Figure 8 for (a) the conventional LSRTM image and (b) the JLSRTM image.

$$\mathrm{S/N} = \frac{P_{\mathrm{signal}}}{P_{\mathrm{noise}}} = \frac{\mathrm{rms}^2_{\mathrm{signal}}}{\mathrm{rms}^2_{\mathrm{noise}}} = 0.3, \tag{12}$$

where P_{signal} denotes the signal power and P_{noise} indicates the noise power. The rms value of noise-free data is 49.7986, and the rms value of noise is 86.3841.

In the inversion procedure, the forward-modeled data are generated by solving the acoustic-wave equation with constant density in equation 1 using a regular-grid finite-difference method. The source wavelet is estimated by averaging the direct arrival at several receivers, the comparison of which to the original Ricker wavelet is shown in Figure 11. The estimated wavelet has a slight phase rotation and ringy side lobes compared with the original Ricker wavelet. This is consistent with 2D propagation and some slight numerical dispersion. The amplitude is normalized to one.

The conventional RTM image is shown in Figure 12a. Because this model contains a very strong vertical velocity gradient, diving waves are present in the recorded data. These waves contribute to imaging the vertical salt flanks in the shallow parts. However, the deep parts of the vertical salt flanks are not well-delineated. Conventional LSRTM improves the resolution and balances the amplitudes of the inverted model, as shown in Figure 12b. JLSRTM can further improve the positioning of the vertical salt flanks by including the contributions of the prismatic reflections. The black arrows in Figure 12 point to density contrasts in the image. The inexact source wavelet has generated severe side lobes associated with each strong reflector, which reduce the resolution of the resulting image.

The magnified views of the gray boxes in Figure 12 are shown in Figure 13, further highlighting the improvements in the image quality and positioning for salt flank delineation with JLSRTM compared to conventional LSRTM. We should note that although the images for conventional LSRTM and JLSRTM become noisy due to random Gaussian noise, density imprints, and imperfect source estimation, JLSRTM still shows its ability to retrieve the steeply dipping structures compared with conventional LSRTM.

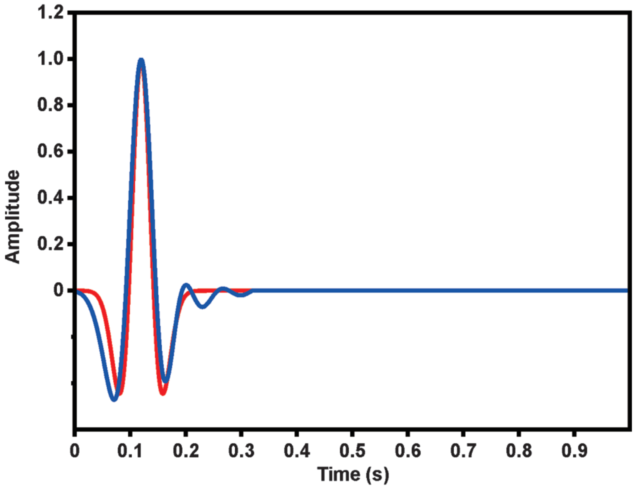

Figure 11. The Ricker wavelet (red) for generating the recorded data and the estimated wavelet (blue) for inversion.

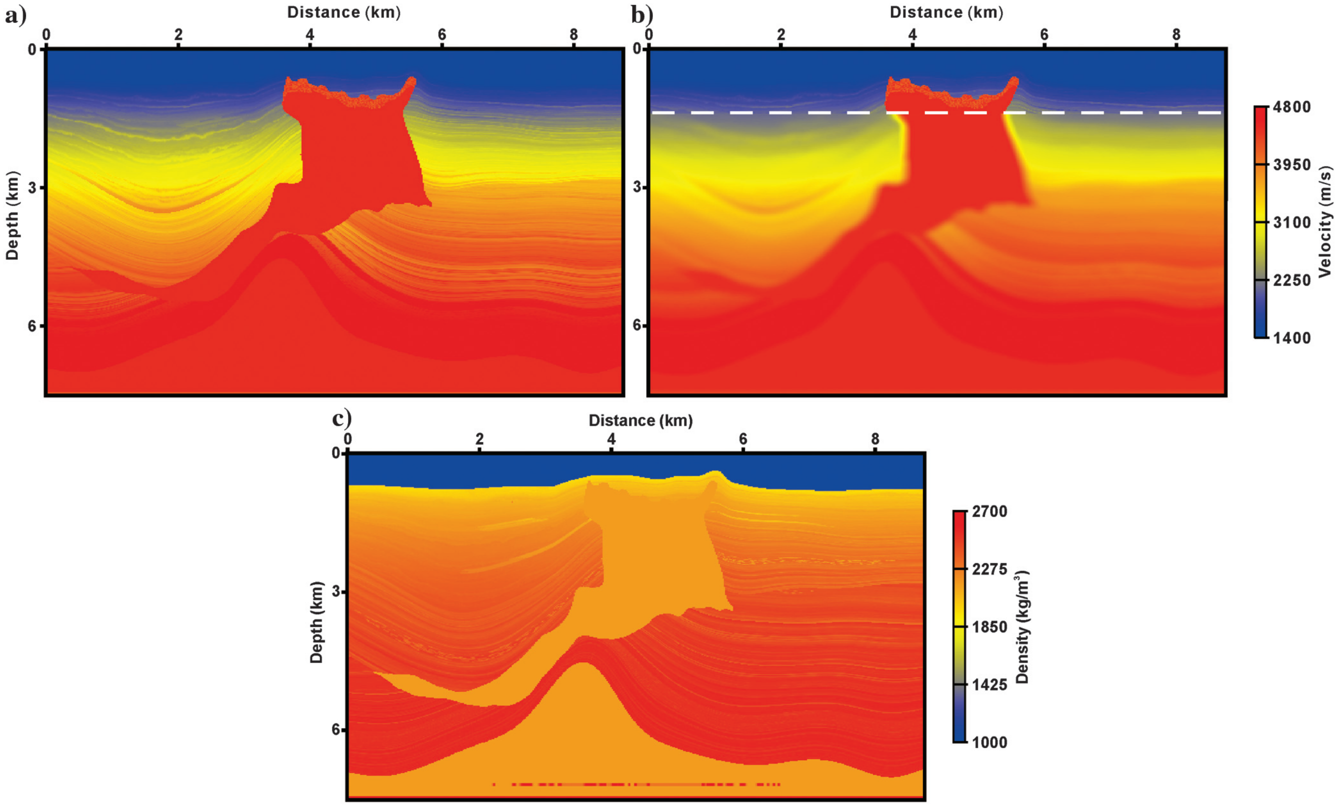

Figure 10. The SEAM model for migration: (a) the true velocity model, (b) the migration velocity model, and (c) the true density model. The density model is only used for generating the recorded data by solving the variable density acoustic-wave equation. The dashed white line indicates the areas in the migration velocity model above this line are fixed as in the true velocity model.

Sensitivity to velocity errors

To quantify the ability of the proposed method to resolve the steeply dipping interfaces in the presence of errors in the migration velocity model, we construct the migration velocity model by scaling the accurate one (Figure 7b) with a factor of 0.95 for the cartoon salt-like model. The final images are shown in Figure 14 for conventional LSRTM and our JLSRTM. Both images become defocused and mispositioned due to the velocity error. The vertical and horizontal reflectors are pulled up because of the slower migration velocity. Nevertheless, the salt flanks are resolved in the JLSRTM image compared with the conventional LSRTM image. These results suggest that the inverted images from JLSRTM degrade as the accuracy of the migration velocity model decreases, similar to conventional LSRTM. However, JLSRTM still has the ability to retrieve the steeply dipping structures despite slight velocity errors.

DISCUSSIONS

The theoretical analyses in Appendices B and C and the numerical examples on the simple L model have clearly shown that direct

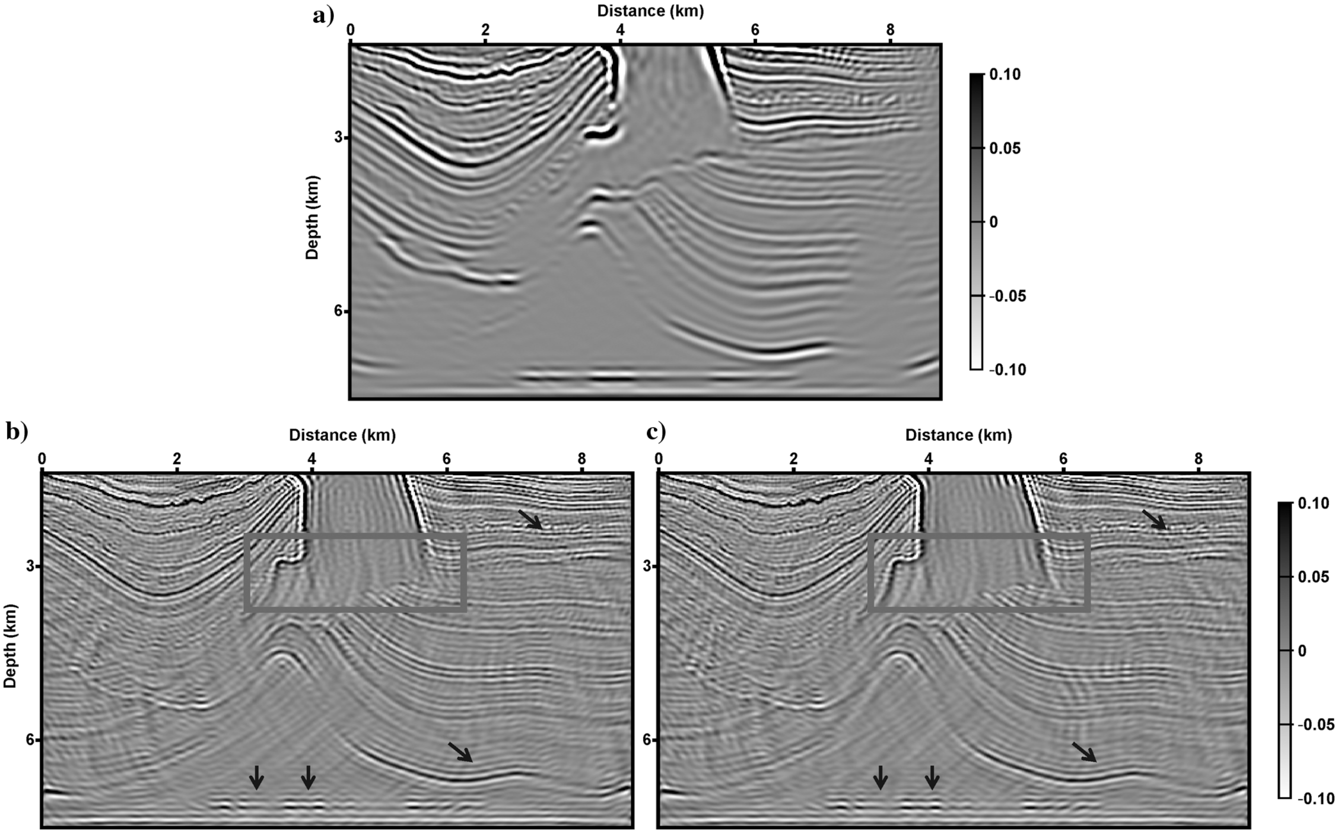

Figure 12. Images from (a) RTM, (b) conventional LSRTM, and (c) JLSRTM for the SEAM model. The black arrows indicate density imprints. The gray boxes point to the areas for the magnified views.

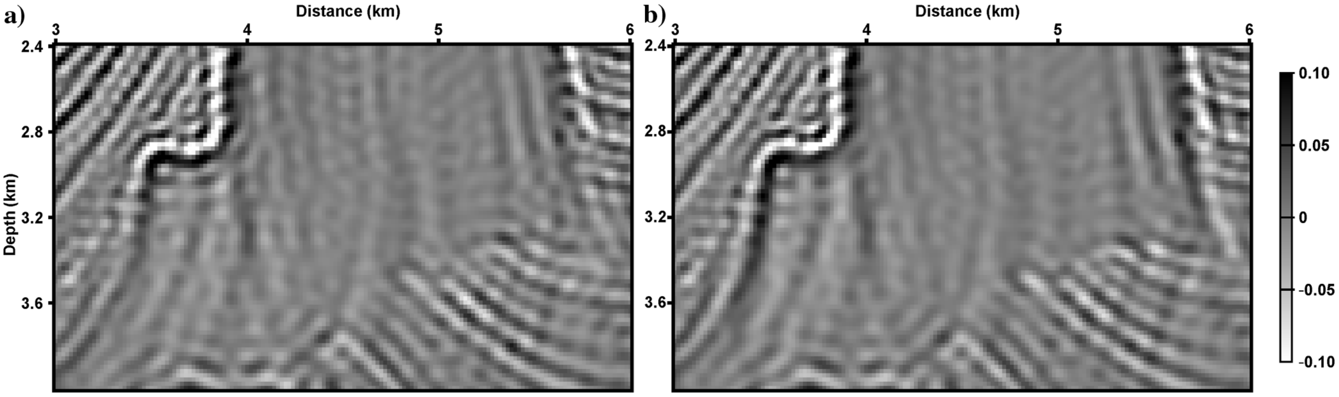

Figure 13. Magnified views of the gray boxes in Figure 12 for (a) the conventional LSRTM image and (b) the JLSRTM image.

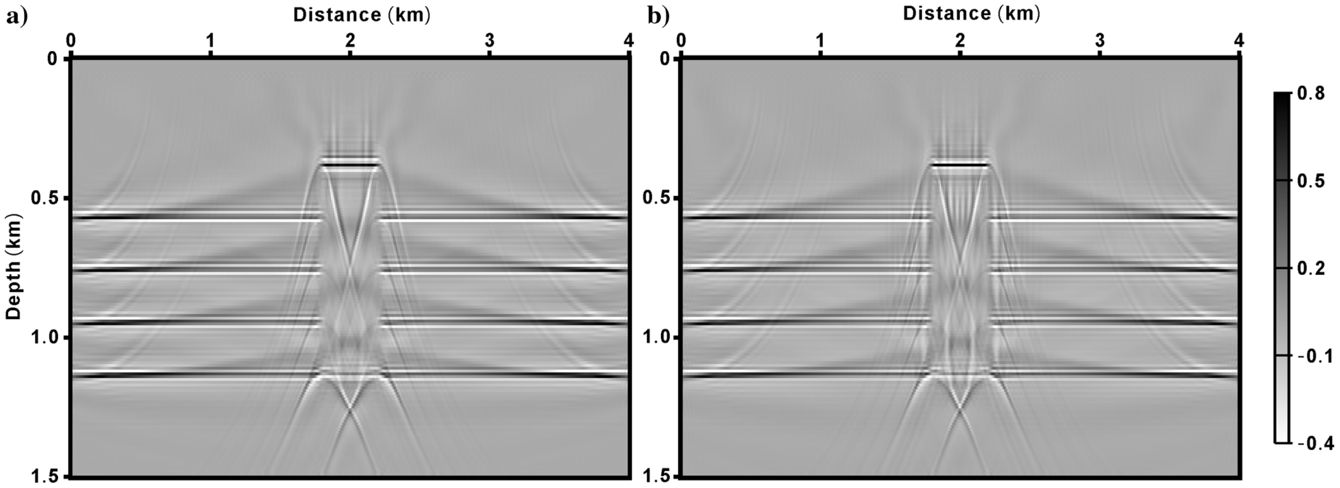

Figure 14. Images from (a) the conventional LSRTM and (b) the JLSRTM for the salt-like model using a migration velocity model by scaling the accurate migration velocity model in Figure 7b with a factor of 0.95.

use of the recorded data for migration could introduce crosstalk artifacts that hamper the iterative inversion process. To provide accurate results, one needs to separate prismatic waves from the recorded data. However, the prediction of prismatic waves is not straightforward. Similar methods proposed previously (Aldawood et al., 2014, 2015) do not discuss how to separate prismatic waves from the recorded data. In this study, we isolate prismatic waves by subtracting the Born modeled data based on the conventional LSRTM image using the recorded data, with the assumption that all of the surface-related and internal multiples are effectively attenuated (Verschuur et al., 1992; Berkhout and Verschuur, 1997; Weglein et al., 1997; Jakubowicz, 1998). For field data applications, however, direct subtraction of the Born modeled data with the recorded field data is a nontrivial task. Special attention, such as source estimation, data normalization, adaptive subtraction, should be taken into account. A more effective and efficient prismatic wave prediction method should be proposed to separate prismatic waves from the recorded data.

Furthermore, noise distribution in field data tends to be non-Gaussian. Coherent noise, such as surface waves and converted waves, will introduce crosstalk artifacts and jeopardize the iterative inversion if they are not effectively attenuated by data processing. Regularization strategies can be introduced to improve the robustness.

The sensitivity tests have demonstrated that our JLSRTM could be sensitive to migration velocity errors, but it can still retrieve the steeply dipping structures despite a slight defocusing and mispositioning. Our experience based on the salt-like model suggests that when the migration velocity errors are more than 10% (with a scaling factor of 0.90), we can barely image the vertical structures. The reasons are twofold: First, the migration images will become blurred when there exist errors in the migration velocity model, and the other is that the prediction of prismatic waves based on the subtraction is unsuccessful. For more complicated velocity models, the upper bound for the velocity errors should be studied in more detail.

CONCLUSION

We have proposed a nonlinear LSRTM scheme for joint inversion of primary and prismatic waves. The output of JLSRTM is a single consistent image that includes structures illuminated by the primary wave and prismatic wave, avoiding the complexities in scaling and/or interpreting the primary and the prismatic images separately. Numerical examples have demonstrated that our JLSRTM has the ability to delineate steeply dipping structures, such as vertical or nearly vertical faults and salt flanks, in which the conventional LSRTM fails. We expect the proposed method to work the best when the prismatic waves are properly predicted, all the surface-related and internal multiples are effectively attenuated, and an accurate migration velocity model is available. Future work will focus on how to correctly predict prismatic waves directly from the recorded data and to improve the robustness when there exist migration velocity errors and noise in the recorded data.

ACKNOWLEDGMENTS

This research was financially supported by the National Natural Science Foundation of China (grant nos. 41474034, 41774122, 41674115, and 41630964), the Strategic Priority Research Program of the Chinese Academy of Sciences (grant no. XDA14010203), the Open Project of the State Key Laboratory of Marine Geology in China (grant no. MGK1808), and the Singapore Economic Development Board Petroleum Engineering Professorship. Y. E. Li and J. Yang also acknowledge the funding of Singapore Ministry of Education Tier-1 grant R-302-000-165-133 and R-302-000-182-114. We would like to thank the assistant editor C. Torres-Verdin, the associate editor J. Schleicher, reviewers R. Coates and C. da Costa, and three anonymous reviewers for their valuable comments and suggestions that helped to improve the manuscript significantly.

APPENDIX A

DERIVATION OF THE NORMAL EQUATION

Following the recipe introduced by Plessix (2006) for adjoint-state method, we define an augmented functional as

$$L(\delta\tilde{u}_1,\delta\tilde{u}_2,\tilde{\lambda},\tilde{\mu},\delta m)=\frac{1}{2}\|R\delta\tilde{u}_1+R\delta\tilde{u}_2-\delta d\|_2^2 \\ -\langle\tilde{\lambda},\Pi_0\delta\tilde{u}_1-\omega^2\delta mu_0\rangle_{\mathbf{U}}-\langle\tilde{\mu},\Pi_0\delta\tilde{u}_2-\omega^2\delta m\delta\tilde{u}_1\rangle_{\mathbf{U}}, \tag{A-1}$$

where $\Pi_0 = -\omega^2 m_0 - \nabla^2$, $\langle , \rangle$ is the scalar product, $\delta\tilde{u}_1$ and $\delta\tilde{u}_2$ are the state variables in space U, and $\tilde{\lambda}$ and $\tilde{\mu}$ are the adjoint-state variables in adjoint space U^*, which satisfy the adjoint-state equations defined by $(\partial L(\delta\tilde{u}_1, \delta\tilde{u}_2, \tilde{\lambda}, \tilde{\mu}, \delta m))/\partial\delta\tilde{u}_1 = 0$ and $(\partial L(\delta\tilde{u}_1, \delta\tilde{u}_2, \tilde{\lambda}, \tilde{\mu}, \delta m))/\partial\delta\tilde{u}_2 = 0$. This gives

$$R^*(R\delta u_1 + R\delta u_2 - \delta d) - \Pi_0^*\lambda + (\omega^2\delta m)^*\mu = 0, \quad \text{(A-2)}$$

$$R^*(R\delta u_1 + R\delta u_2 - \delta d) - \Pi_0^*\mu = 0, \quad \text{(A-3)}$$

where $*$ denotes the adjoint operator and R^* denotes spreading the recorded data at the receiver location to the whole model space, in which the nonreceiver locations are filled with zero. The gradient of the objective function in equation 9 with respect to the model parameter δm can be obtained by

$$\frac{\partial J}{\partial \delta m} = \frac{\partial L(\delta\tilde{u}_1, \delta\tilde{u}_2, \tilde{\lambda}, \tilde{\mu}, \delta m)}{\partial \delta m} = (\omega^2 u_0)^*\lambda + (\omega^2\delta u_1)^*\mu. \quad \text{(A-4)}$$

The minimizer of equation 9 can be found by setting the gradient in equation A-4 to zero, resulting in the following normal equation:

$$H\delta m = m_{\text{mig}}, \quad \text{(A-5)}$$

where $H\delta m$ and m_{mig} are satisfying:

$$H\delta m = (\omega^2 u_0)^*\lambda_1 + (\omega^2\delta u_1)^*\mu, \quad \text{(A-6)}$$

$$m_{\text{mig}} = (\omega^2 u_0)^*\lambda_2. \quad \text{(A-7)}$$

In equations A-6 and A-7, λ_1 and λ_2 are the solutions of

$$\Pi_0^*\lambda_1 = R^*(R\delta u_1 + R\delta u_2) + (\omega^2\delta m)^*\mu, \quad \text{(A-8)}$$

$$\Pi_0^*\lambda_2 = R^*\delta d, \quad \text{(A-9)}$$

wherein $\lambda = \lambda_1 - \lambda_2$ is the solution of equation A-2.

APPENDIX B

IMAGING CONDITION FOR MIGRATION OF PRISMATIC WAVES

Jin et al. (2006) define the imaging condition for migration of prismatic waves as the crosscorrelation of the source-side downgoing wave and the receiver-side upgoing wave plus the crosscorrelation of the source-side upgoing wave and the receiver-side downgoing wave. However, such an imaging term may appear as low-wavenumber noises in conventional RTM (Liu et al., 2011). Here, we reformulate this imaging condition by analyzing the gradient in equation A-4.

Writing out the terms in equation A-4 explicitly, we get

$$(\omega^2 u_0)^*\lambda + (\omega^2\delta u_1)^*\mu = (\omega^2 u_0)^*(\Pi_0^*)^{-1}R^*(R\delta u_1 - \delta d_1) \quad \text{(B-1)}$$

$$+(\omega^2 u_0)^*(\Pi_0^*)^{-1}R^*(R\delta u_2 - \delta d_2) \quad \text{(B-2)}$$

$$+(\omega^2 u_0)^*(\Pi_0^*)^{-1}[(\omega^2\delta m)^*(\Pi_0^*)^{-1}R^*(R\delta u_1 - \delta d_1)] \quad \text{(B-3)}$$

$$+(\omega^2 u_0)^*(\Pi_0^*)^{-1}[(\omega^2\delta m)^*(\Pi_0^*)^{-1}R^*(R\delta u_2 - \delta d_2)] \quad \text{(B-4)}$$

$$+(\omega^2\delta u_1)^*(\Pi_0^*)^{-1}R^*(R\delta u_1 - \delta d_1) \quad \text{(B-5)}$$

$$+(\omega^2\delta u_1)^*(\Pi_0^*)^{-1}R^*(R\delta u_2 - \delta d_2). \quad \text{(B-6)}$$

The term on the right side of equation B-1 corresponds to the migration of primary waves, and this is what we want in conventional RTM. The term in equation B-2 stands for that the prismatic waves are migrated as primary waves, and it is considered as noise for conventional RTM. The terms in equations B-3 and B-5 are the imaging condition for down-/up- and up-/downgoing waves, and these terms are responsible for the low-wavenumber noise in conventional RTM (Liu et al., 2011). They will also generate artifacts at the same location as the right side term in equation B-1 with a different polarity. These artifacts are also illustrated in Figure 5a. The terms in equations B-4 and B-6 correspond to the imaging condition for migration of prismatic waves in which the singly scattered wavepaths and the double scattered data are correctly accounted for. Similar analyses can be found in Dai and Schuster (2013).

APPENDIX C

REFORMULATION OF THE NORMAL EQUATION

Writing out the terms of $H\delta m$ in equation A-6 explicitly, we get the first term

$$(\omega^2 u_0)^*\lambda_1 = (\omega^2 u_0)^*(\Pi_0^*)^{-1}R^*(R\delta u_1) \quad \text{(C-1)}$$

$$+(\omega^2 u_0)^*(\Pi_0^*)^{-1}R^*(R\delta u_2) \quad \text{(C-2)}$$

$$+(\omega^2 u_0)^*(\Pi_0^*)^{-1}[(\omega^2\delta m)^*(\Pi_0^*)^{-1}R^*(R\delta u_1)] \quad \text{(C-3)}$$

$$+(\omega^2 u_0)^*(\Pi_0^*)^{-1}[(\omega^2\delta m)^*(\Pi_0^*)^{-1}R^*(R\delta u_2)] \quad \text{(C-4)}$$

$$-(\omega^2 u_0)^*(\Pi_0^*)^{-1}[(\omega^2\delta m)^*(\Pi_0^*)^{-1}R^*\delta d_1] \quad \text{(C-5)}$$

$$-(\omega^2 u_0)^*(\Pi_0^*)^{-1}[(\omega^2\delta m)^*(\Pi_0^*)^{-1}R^*\delta d_2], \quad \text{(C-6)}$$

and the second term

$$(\omega^2\delta u_1)^*\mu = (\omega^2\delta u_1)^*(\Pi_0^*)^{-1}R^*(R\delta u_1) \quad \text{(C-7)}$$

$$+(\omega^2\delta u_1)^*(\Pi_0^*)^{-1}R^*(R\delta u_2) \quad \text{(C-8)}$$

$$-(\omega^2\delta u_1)^*(\Pi_0^*)^{-1}R^*\delta d_1 \quad \text{(C-9)}$$

$$-(\omega^2\delta u_1)^*(\Pi_0^*)^{-1}R^*\delta d_2. \quad \text{(C-10)}$$

According to the analyses in Appendix A, the terms in equations C-2, C-3, C-5, C-7, and C-9 are crosstalk artifacts and they

Algorithm C-1. Hessian-vector product implementation procedure.

1) Forward propagation with the background velocity model to obtain u_0 using equation C-11.
2) Forward propagation using $\omega^2 p_k u_0$ as the source to obtain δu_1 and $R\delta u_1$ using equation C-12.
3) Backpropagation of the observed prismatic wave δd_2 to obtain μ using equation C-13.
4) Backpropagation using $R^*(R\delta u_1) - (\omega^2 p_k)^* \mu$ as the source to obtain λ_1 using equation C-14.
5) Calculation of Hessian-vector product Hp_k using equation C-16.

can be explicitly dropped off because we have assumed that prismatic waves δd_2 can be isolated from the recorded data δd. In addition, the terms in equations C-4 and C-8 are nonlinear terms. By dropping off these two terms, we are making a linearization approximation, and the computational cost is thus reduced.

After removing the crosstalk artifacts and nonlinear terms, the normal equation can be reformulated as follows:

$$\Pi_0 u_0 = f, \tag{C-11}$$

$$\Pi_0 \delta u_1 = \omega^2 \delta m u_0, \tag{C-12}$$

$$\Pi_0^* \mu = R^* \delta d_2, \tag{C-13}$$

$$\Pi_0^* \lambda_1 = R^*(R\delta u_1) - (\omega^2 \delta m)^* \mu, \tag{C-14}$$

$$\Pi_0^* \lambda_2 = R^* \delta d, \tag{C-15}$$

$$H\delta m = (\omega^2 u_0)^* \lambda_1 + (\omega^2 \delta u_1)^* \mu, \tag{C-16}$$

$$m_{\mathrm{mig}} = (\omega^2 u_0)^* \lambda_2. \tag{C-17}$$

This procedure is similar to Métivier et al. (2017, their equations 3.12, 3.13, 3.22 to 3.24). The main difference is that we only use the prismatic wave δd_2 for backpropagation in calculating $H\delta m$ to eliminate the crosstalk artifacts, whereas Métivier et al. (2017) use the whole observed data δd including the primary wave δd_1 and the prismatic wave δd_2. To calculate the Hessian-vector product $H\delta m$, four simulation problems need to be solved to obtain the wavefields $u_0, \delta u_1, \mu, \lambda_1$. The computational cost here relies on the assumption that isolation of prismatic waves from the recorded data is readily available. We should also keep in mind the extra computational cost needed for isolation of prismatic waves.

The reformulated normal equation can be iteratively solved by a conjugate gradient algorithm (Hestenes and Stiefel, 1952). At each iteration, we only need to calculate the Hessian-vector product Hp_k, where p_k is an arbitrary model vector. This can be obtained by replacing δm with p_k in equations C-11–C-16. The detailed implementation procedures for calculating Hp_k are listed in Algorithm C-1.

REFERENCES

Aldawood, A., I. Hoteit, G. Turkiyyah, M. Zuberi, and T. Alkhalifah, 2014, Linearized least-square imaging of internally scattered data: 76th Annual International Conference and Exhibition, EAGE, Extended Abstracts, We G103 110, doi: 10.3997/2214-4609.20141160.

Aldawood, A., I. Hoteit, M. Zuberi, G. Turkiyyah, and T. AlKhalifah, 2015, The possibilities of least-squares migration of internally scattered seismic energy: Geophysics, **80**, no. 4, S93–S101, doi: 10.1190/geo2014-0436.1.

Berkhout, A. J., and D. Verschuur, 1997, Estimation of multiple scattering by iterative inversion, Part I: Theoretical considerations: Geophysics, **62**, 1586–1595, doi: 10.1190/1.1444261.

Claerbout, J. F. 1992, Earth soundings analysis: Processing versus inversion: Blackwell Scientific Publications.

Dai, W., and G. T. Schuster, 2013, Reverse time migration of prism waves for salt flank delineation: 83rd Annual International Meeting, SEG, Expanded Abstracts, 3861–3865, doi: 10.1190/segam2013-0414.1.

Farmer, P. A., I. F. Jones, H. Zhou, R. I. Bloor, and M. C. Goodwin, 2006, Application of reverse time migration to complex imaging problems: First Break, **24**, no. 9, 65–73.

Fehler, M., and P. J. Keliher, 2011, SEAM Phase 1: Challenges of subsalt imaging in tertiary basins, with emphasis on deepwater Gulf of Mexico: SEG.

Hale, D., N. R. Hill, and J. Stefani, 1992, Imaging salt with turning seismic waves: Geophysics, **57**, 1453–1462, doi: 10.1190/1.1443213.

Hestenes, M. R., and E. Stiefel, 1952, Methods of conjugate gradients for solving linear systems: Journal of Research of the National Bureau of Standards, **49**, 409, doi: 10.6028/jres.049.044.

Hu, W., A. Abubakar, and T. M. Habashy, 2007, Application of the nearly perfectly matched layer in acoustic wave modeling: Geophysics, **72**, no. 5, SM169–SM175, doi: 10.1190/1.2738553.

Jakubowicz, H., 1998, Wave equation prediction and removal of interbed multiples: 68th Annual International Meeting, SEG, Expanded Abstracts, 1527–1530, doi: 10.1190/1.1820204.

Jin, S., S. Xu, and D. Walraven, 2006, One-return wave equation migration: Imaging of duplex waves: 76th Annual International Meeting, SEG, Expanded Abstracts, 2338–2342, doi: 10.1190/1.2370003.

Jones, I. F., M. C. Goodwin, I. D. Berranger, H. Zhou, and P. A. Farmer, 2007, Application of anisotropic 3D reverse time migration to complex North Sea imaging: 77th Annual International Meeting, SEG, Expanded Abstracts, 2140–2144, doi: 10.1190/1.2792911.

Li, Y., Y. Agnihotri, and T. Dy, 2011, Prismatic wave imaging with dual flood RTM: 81st Annual International Meeting, SEG, Expanded Abstracts, 3290–3294, doi: 10.1190/1.3627879.

Liu, F., G. Zhang, S. A. Morton, and J. P. Leveille, 2011, An effective imaging condition for reverse-time migration using wavefield decomposition: Geophysics, **76**, no. 1, S29–S39, doi: 10.1190/1.2792917.

Malcolm, A. E., M. V. De Hoop, and B. Ursin, 2011, Recursive imaging with multiply scattered waves using partial image regularization: A North Sea case study: Geophysics, **76**, no. 2, B33–B42, doi: 10.1190/1.3537822.

Malcolm, A. E., B. Ursin, and V. Maarten, 2009, Seismic imaging and illumination with internal multiples: Geophysical Journal International, **176**, 847–864, doi: 10.1111/j.1365-246X.2008.03992.x.

Marmalyevskyy, N., Y. Roganov, Z. Gornyak, A. Kostyukevych, and V. Mershchiy, 2005, Migration of duplex waves: 75th Annual International Meeting, SEG, Expanded Abstracts, 2025–2028, doi: 10.1190/1.2148107.

Métivier, L., R. Brossier, S. Operto, and J. Virieux, 2017, Full waveform inversion and the truncated Newton method: SIAM Review, **59**, 153–195, doi: 10.1137/16M1093239.

Plessix, R. -E., 2006, A review of the adjoint-state method for computing the gradient of a functional with geophysical applications: Geophysical Journal International, **167**, 495–503.

Tan, S., and L. Huang, 2014, Least-squares reverse-time migration with a wavefield-separation imaging condition and updated source wavefields: Geophysics, **79**, no. 5, S195–S205, doi: 10.1190/geo2014-0020.1.

Verschuur, D. J., A. Berkhout, and C. Wapenaar, 1992, Adaptive surface-related multiple elimination: Geophysics, **57**, 1166–1177, doi: 10.1190/1.1443330.

Weglein, A. B., F. A. Gasparotto, P. M. Carvalho, and R. H. Stolt, 1997, An inverse-scattering series method for attenuating multiples in seismic reflection data: Geophysics, **62**, 1975–1989, doi: 10.1190/1.1444298.

Xu, S., and S. Jin, 2006, Wave equation migration of turning waves: 76th Annual International Meeting, SEG, Expanded Abstracts, 2328–2332, doi: 10.1190/1.2370001.

Zuberi, M., and T. Alkhalifah, 2013, Selective interferometric imaging of internal multiples: 75th Annual International Conference and Exhibition, EAGE, Extended Abstracts, Th 15 16, doi: 10.3997/2214-4609.20130197.

Zuberi, M. A. H., and T. Alkhalifah, 2014, Generalized internal multiple imaging: Geophysics, **79**, no. 5, S207–S216, doi: 10.1190/geo2013-0287.1.